Working Paper No.
2026-06

INET Oxford Working Paper Series
20 February 2026

The Convexity of Hurricane Damages

François Cohen, Luis Sarmiento, and Yannik Stuka

The Convexity of Hurricane Damages

François Cohen[1,2], Luis Sarmiento[3,4,5,6], Yannik Stuka[1,3,4,7]

Authors in alphabetical order (contact: yannikjosef.stuka@unive.it)

February 20, 2026

Abstract

Most economic studies of environmental disasters focus on event occurrence, typically using difference-in-differences methods. However, intensity is often the more relevant margin. We study hurricanes, whose intensity is projected to increase with climate change while changes in frequency remain uncertain. We exploit spatial asymmetries in storm dynamics to causally identify how damages vary with intensity. In the Northern Hemisphere, translational and rotational winds reinforce each other on the right side of storms, creating a natural fuzzy discontinuity. In addition, short-run fluctuations in the position of the Bermuda High, a large high-pressure system over the Atlantic, influence hurricane trajectories near the U.S. coast, generating quasi-random variation in regional exposure. In this preliminary draft, we show how these physical mechanisms can be used to identify exogenous variation in hurricane intensity at the local level, laying the groundwork for estimating how damages scale with intensity in future iterations of this working paper.

Keywords: Hurricanes; Intensity; Asymmetry; Convexity; Damages; United States.

JEL Classification Numbers: Q51, Q54.

We thank the participants of the EAERE 2025, SAEe 2025 and IAERE 2026 conferences, and the Internal PhD Seminar Series of UB and Ca' Foscari for their valuable feedback.

[1]University of Barcelona, Chair of Energy Sustainability and Institute of Economics of Barcelona, Spain.
[2]Institute for New Economic Thinking, University of Oxford.
[3]CMCC – Euro-Mediterranean Center on Climate Change.
[4]EIEE – European Institute on Economics and the Environment.
[5]Banco de México, Mexico.
[6]Department of Management, Technology, and Economics, ETH Zurich
[7]Ca' Foscari University of Venice, Italy.

1 Introduction

Most of the economic literature on environmental disasters focuses on the occurrence of events, typically relying on difference-in-differences designs to identify average treatment effects.[1] However, for climate and adaptation policy, changes in intensity rather than frequency are often the more relevant margin.

Hurricanes, which cost billions of dollars to the U.S. economy alone, are a particularly clear example. While there is no robust evidence that climate change increases hurricane frequency, hurricane intensity is projected to rise with high confidence, driven by warmer ocean conditions (Lugo, 2000; Holland and Bruyère, 2014; Mudd et al., 2014).

The importance of intensity extends beyond hurricanes to other disasters, such as floods, droughts, and forest fires, whose damages can differ markedly across settings (Cavallo and Noy, 2010; Kellenberg and Mobarak, 2011). At the macroeconomic level, this difficulty in identifying how damages scale with intensity implies that the curvature of the climate damage function remains poorly identified. As a result, climate–economy models often rely on simplified and weakly tested functional forms, such as quadratic damages (Nordhaus, 2018; Barrage and Nordhaus, 2024), which may understate convexity for the most pessimistic scenarios (Weitzman, 2012; Dietz and Stern, 2015).

In this preliminary draft, we exploit spatial asymmetries in geophysical processes to generate plausibly exogenous variation in hurricane intensity. We only establish the physical and econometric foundations. We will estimate the nonlinear intensity-damage relationship in future iterations of this working paper.

Our identification strategy will exploit two structural features of storms. In the Northern Hemisphere, tropical storms rotate counterclockwise and also typically move northward, generating systematic asymmetries in surface wind intensity. The storm's northward motion reinforces rotational winds on the right-hand side of the storm, relative to the direction of

[1] Most analyses exploit the localised nature of disasters to construct treated and control areas within event-study frameworks. This approach is used, for example, by Xiao (2011); Barone and Mocetti (2014); Deryugina (2017); Paudel and Ryu (2018); Karbownik and Wray (2019); Sheldon and Zhan (2019); Masiero and Santarossa (2021); Roth Tran and Wilson (2025).

motion, and partially offsets them on the left-hand side (Willoughby et al., 2006; Powell et al., 2003; Uhlhorn et al., 2014). This asymmetry creates a natural fuzzy discontinuity, whereby locations on one side of the storm experience systematically stronger winds than those on the other.

In addition, hurricane trajectories are highly sensitive to high-altitude wind patterns that are difficult to predict. In the United States, sudden shifts in the Bermuda High, a high-altitude pressure system over the central Atlantic, can push hurricanes eastward or northward (Knowles and Leitner, 2007; Cappucci and Noll, 2025), generating plausibly exogenous variation in storm trajectories.

In this early draft, we first present the physical mechanisms used for identification, and then first stage results. We then confirm substantial differences in wind strength between the left- and right-hand sides of storms, as well as their relevance to study the impact of changes in hurricane intensity. We finally show that Bermuda High movements can explain regional differences in storm exposure. The full paper will analyse damages and their convexity as a function of storm intensity.

2 Physical Mechanisms Underlying Identification

From 1980 to 2023, tropical cyclones caused about $1.5 trillion in inflation-adjusted direct damages in the U.S., representing more than half of all losses from billion-dollar disasters over this period (NOAA National Centers for Environmental Information, 2025). Tropical cyclones vary widely in intensity. Meteorologists classify them as tropical depressions, tropical storms, or hurricanes based on their maximum sustained wind speed. Hurricanes are further categorized using the Saffir–Simpson Hurricane Wind Scale (SSHWS), which ranks them from Category 1 to Category 5 according to maximum sustained wind speed. (National Hurricane Center, 2026).[2] Large, single events can result in $20 to $30 billion in losses, far exceeding typical floods or wildfires. Some individual storms have caused damages in the hundreds of billions, with Hurricane Katrina (2005) being the costliest U.S. hurricane on record, with estimated total losses of around $186 billion in 2022 dollars (Center for Climate and Energy Solutions, 2026).[3]

Four components determine the wind intensities experienced during a tropical cyclone at a given location: the storm's intensity, the distance relative to the storm's eye, the storm's rotational winds, and its forward (translational) motion.

Wind speeds are typically strongest over the ocean and at landfall, after which they progressively weaken as the hurricane moves inland across the United States. Furthermore, winds are calm within the eye of the storm, peak in intensity in the eyewall, and generally weaken with distance from the storm's centre (Willoughby et al., 2006).

[2]Tropical depressions have maximum sustained surface wind speeds of 38 mph (62 km/h) or less, tropical storms range from 39–73 mph (63–118 km/h), and hurricanes are classified into Categories 1–5 under the Saffir–Simpson Hurricane Wind Scale. Category 1 corresponds to 74–95 mph (119–153 km/h), Category 2 to 96–110 mph (154–177 km/h), Category 3 to 111–129 mph (178–208 km/h), Category 4 to 130–156 mph (209–251 km/h), and Category 5 to 157 mph (252 km/h) or higher. Major hurricanes are category 3 and above (National Hurricane Center, 2026; NASA, 2022). Besides, hurricane is the regional name used in the North Atlantic and Eastern North Pacific. The same phenomenon is referred to as a typhoon in the Western North Pacific and simply as a tropical cyclone elsewhere (NASA, 2022).

[3]In 2017, Hurricane Harvey caused approximately $125 billion in damage through record flooding in the Houston area, Hurricane Maria devastated Puerto Rico with around $100 billion in losses and a severe humanitarian crisis, and Hurricane Irma caused roughly $50 billion in damage across the Caribbean and Florida. Four of the ten costliest U.S. hurricanes on record occurred in just 2017 and 2018 (Center for Climate and Energy Solutions, 2026). More recently, Hurricanes Ida (2021) and Ian (2022) each caused tens of billions of dollars in damage.

Winds are primarily rotational. In the Northern Hemisphere, hurricanes rotate counterclockwise as a result of the Earth's rotation.[4] As a consequence, rotational winds typically blow from north to south on the left-hand side of the storm and in the opposite direction on the right-hand side.

Wind intensity is further shaped by a cyclone's translational movement (Wang Bin et al., 1999; Chan, 2005). Once a tropical cyclone has formed, its subsequent movement is largely determined by large-scale atmospheric steering currents (Wang Bin et al., 1999; Chan, 2005). Storm motion can be understood as that of a rotating cylinder carried along by surrounding winds. In the United States, hurricanes typically travel hundreds of kilometres northward or northwestward. The easterly trade winds and the Bermuda High (Knowles and Leitner, 2007; Cappucci and Noll, 2025) steer hurricanes along their trajectories. This forward motion reinforces rotational winds on the right-hand side of the storm and partially offsets them on the left-hand side, creating a systematic asymmetry in wind intensity across the storm track (Willoughby et al., 2006; Uhlhorn et al., 2014).

This left–right asymmetry is represented in Figure 1 (panel a). In addition, panel (b) represents the steering effect of the Bermuda High (BH). The Bermuda High is a large high-pressure area that can be understood as a dome with clockwise wind circulation. Because tropical cyclones are steered by the surrounding large-scale winds, they tend to move along the edge of this pressure system. When the high shifts position, often tracked using the ridge centroid, the path of approaching storms shifts accordingly, altering where they make landfall and which regions are exposed. Therefore, short-run fluctuations in the Bermuda High play a determinant role in steering Atlantic hurricanes near the U.S. coast. When the high extends farther west, storms tend to travel farther west before turning. When it is weaker or shifted east, storms turn north earlier. Ultimately, short-run variations in the position and strength of the Bermuda High at the time when a tropical cyclone approaches the U.S. coast can cause storm tracks to curve northward or northeastward (Knowles and

[4] As air flows over long distances toward the low-pressure centre of the storm, it is deflected by the Earth's rotation, causing it to follow a curved trajectory. This Coriolis effect leads tropical cyclones to rotate counterclockwise in the Northern Hemisphere and clockwise in the Southern Hemisphere (NASA, 2022).

Leitner, 2007; Cappucci and Noll, 2025), thereby shaping landfall locations.

BH steering operates at short time scales. Other atmospheric phenomena have more structural influences. For example, the El Niño–Southern Oscillation has global impacts on weather patterns and affects both storm activity and economic conditions in the United States (Cashin et al., 2017). In contrast, short-run fluctuations in the Bermuda High during the days when tropical cyclones approach the U.S. coast can steer storms toward or away from the United States while having little direct relevance for contemporaneous U.S. economic activity.[5] Importantly, BH steering does not determine storm formation, which typically occurs thousands of kilometers away.

Figure 1: Stylised representation of storm movements and asymmetries.

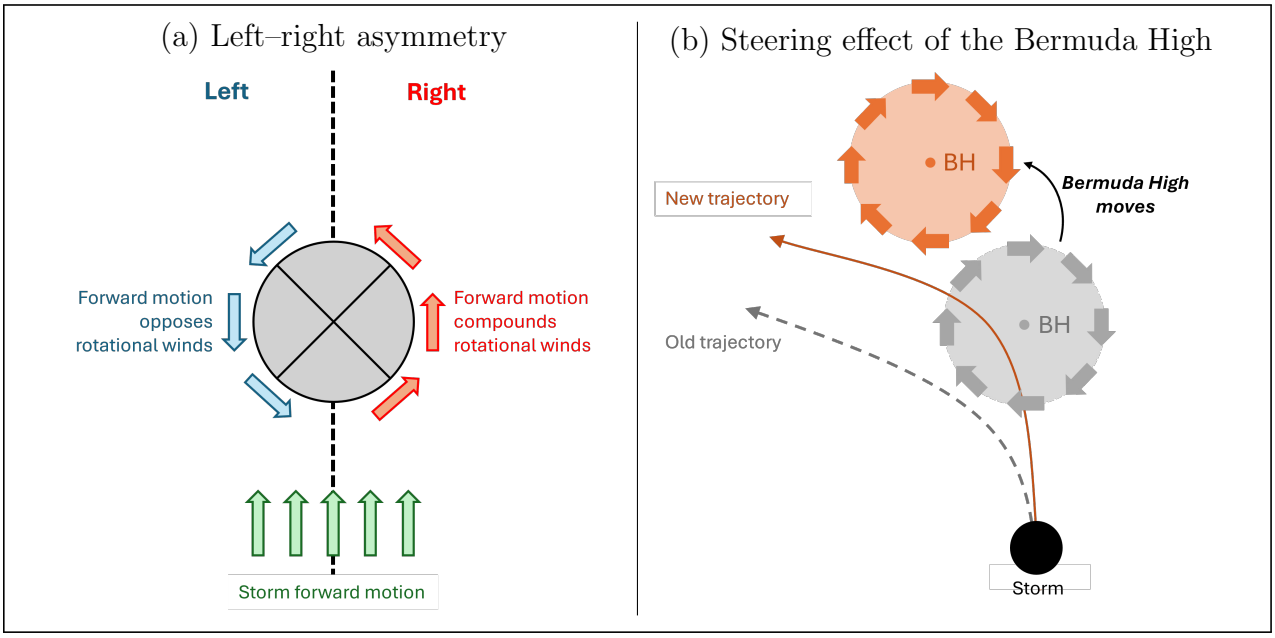

Source: Authors' own construction. Panel (a) illustrates how storm forward motion combines with counterclockwise rotational winds to produce stronger realized winds on the right-hand side of the track and weaker winds on the left-hand side. Panel (b) illustrates how shifts in Bermuda High position alter hurricane trajectories and spatial exposure in a nonlinear way.

[5]Seasonal patterns in the Bermuda High do affect precipitation and humidity in the United States (Diem, 2013; Zhu and Liang, 2013). This is why, in this paper, we only rely on short-term shifts in the Bermuda High, which are unlikely to generate persistent or structural differences across U.S. regions.

3 Impact of Physical Mechanisms on the Intensity of Tropical Cyclones

This section shows that left–right asymmetries and shifts in the Bermuda High generate plausibly exogenous variation in tropical cyclone intensity, as measured by wind speed and precipitation.

3.1 Measurement of Left–Right Exposure

We use the North Atlantic Hurricane Database version 2 (HURDAT2) (NOAA National Hurricane Center, 2024; Landsea and Franklin, 2013) to track tropical cyclone trajectories. HURDAT2 provides 6-hourly observations for all tropical and subtropical cyclones in the North Atlantic basin, including storm-center locations, maximum sustained wind speeds, and minimum central pressures. Our sample includes all storms originating in the Atlantic basin between 2000 and 2023. It covers 428 tropical cyclones: 8% remained at the level of tropical depressions (maximum sustained wind speed below 38 mph), 48% reached tropical storm intensity (39-73 mph) and 44% became hurricanes (74 mph and above).

We spatially match tropical cyclone tracks to U.S. counties using population-weighted county centroid coordinates from the U.S. Census Bureau Centers of Population files (U.S. Census Bureau, 2011), accessed via the `USpopcenters` R package (Krieger, 2023), and county boundary shapefiles from the U.S. Census Bureau (U.S. Census Bureau, 2018). This procedure allows us to compute, for each county, the number of times it lay within 300 km of a tropical cyclone track (Figure 2, panel a). Specifically, for each storm we construct a 300 km buffer around its trajectory and record whether the buffer covers the county centroid. Figure 2 (panel b) illustrates this procedure for Tropical Storm Arlene. We typically find that counties in the Southeastern United States are substantially more exposed to tropical cyclone strikes.

We classify each storm–county pair according to whether the county lies to the left or to the right of the storm center relative to the direction of storm motion (Figure 2, panel c). Unlike overall exposure, left- and right-hand strikes are much more evenly distributed across

counties, substantially reducing geographical sorting. Left-hand strikes account for 61% of all strikes, largely because tropical cyclones frequently track close to the U.S. East Coast. Figure 2 (panel d) further identifies counties that experienced balanced exposure from left- and right-hand strikes.

Figure 2: **Tropical cyclone exposure measures at the county level.**

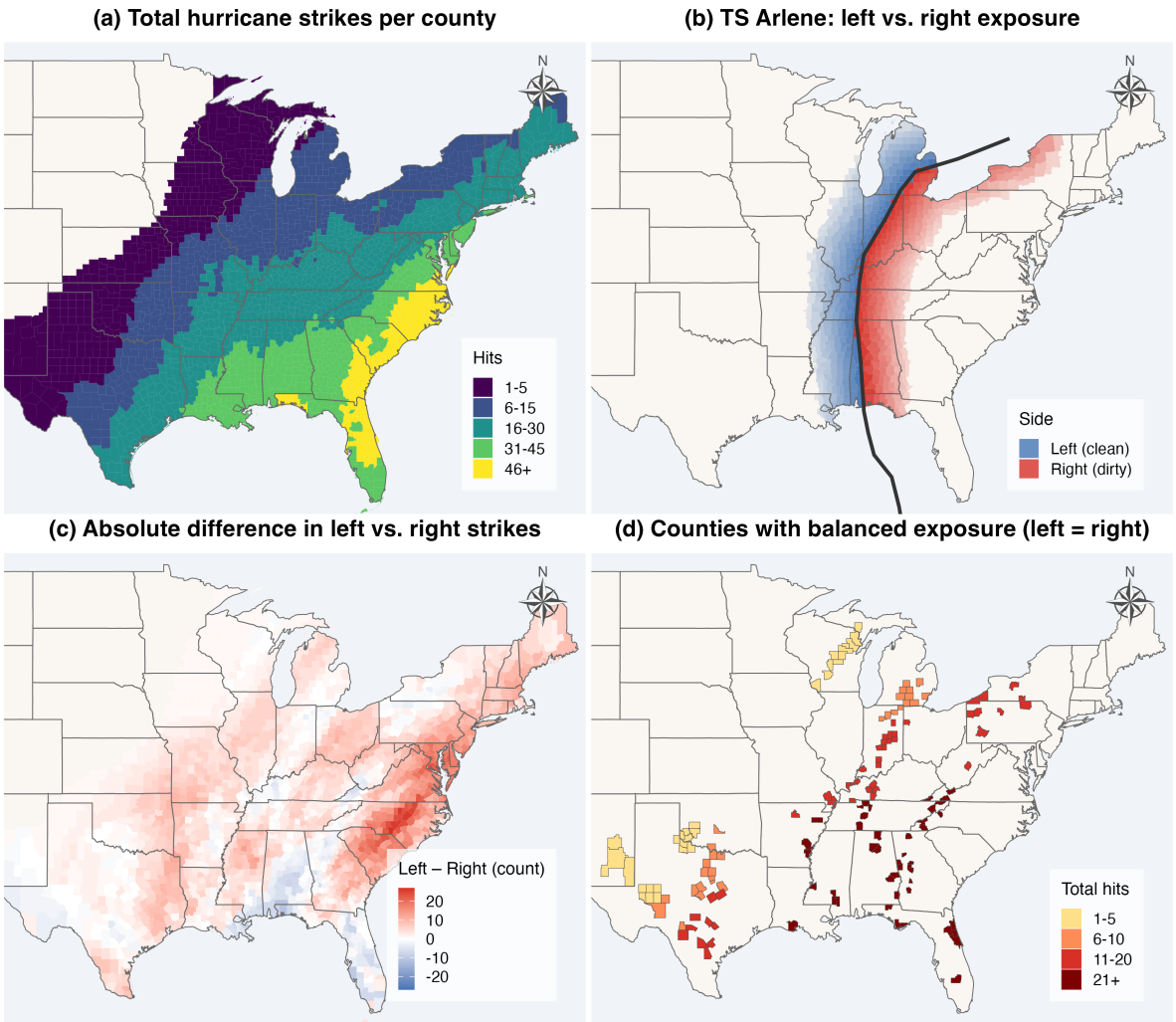

Notes: Panel (a): tropical cyclone strikes within 300 km of the track. Panel (b): Tropical Storm Arlene, colored by left (clean) vs. right (dirty) side. Panel (c): absolute difference in left- and right-side strikes (red = more left, blue = more right). Panel (d): counties with balanced left–right exposure, colored by total hits.

3.2 Left–right asymmetries in wind and precipitation

To characterize asymmetries in wind and precipitation between the left- and right-hand sides of tropical cyclones, we primarily draw on modeled data aggregated at the county level. Modeled data are preferable for measuring storm intensity because observational coverage is spatially uneven and often sparse in areas most affected by tropical cyclones. In addition, modeled products integrate multiple observational sources, reducing measurement bias that may arise from reliance on a single instrument.

We obtain county-level wind exposure by applying a parametric tropical cyclone wind-field model (Holland, 1980) implemented in the `stormwindmodel` R package (Anderson et al., 2021) to HURDAT2 best-track data and interpolating modeled 10-meter, 1-minute sustained wind speeds to county population-weighted centroids. The resulting dataset provides continuous county-level estimates of maximum sustained surface wind speeds for each Atlantic-basin tropical cyclone from 2000 to 2023.

We further obtain county-level measures of storm-related precipitation from the PRISM Climate Group's daily precipitation grids (PRISM Climate Group, 2024) accessed via the `prism` R package (Hart and Bell, 2015).[6] We aggregate daily precipitation to compute total storm-period rainfall for a period spanning 7 days around the storm's closest approach to each county.

We complement modeled products with direct meteorological observations from weather stations. We use hourly records from the NOAA Integrated Surface Database (ISD) Lite product, which provides quality-controlled hourly measurements from surface weather stations worldwide (Smith et al., 2011). We retrieve data for all U.S. stations active during the period 2000–2025, accessed via the ISD-Lite archive distributed by NOAA's National Centers for Environmental Information (NCEI). Variables include air temperature (°C), wind

[6]PRISM (Parameter-elevation Regressions on Independent Slopes Model) produces spatially continuous precipitation estimates at 4 km resolution for the contiguous United States by interpolating station observations using a climate-informed regression framework that accounts for elevation, coastal proximity, and orographic effects. We aggregate the data at the county level by taking the mean of the grid points that fall within the respective county boundaries such that for each county–storm pair the dataset reports average total accumulated precipitation for each storm day.

speed (m/s), wind direction (degrees), sea-level pressure (hPa), and precipitation (mm, at 1-hour and 6-hour accumulations). For each station–storm pair, we compute rolling-window statistics centered on the time of the storm's closest approach: the maximum wind speed and accumulated rainfall over 24-hour, 72-hour, and 168-hour (7-day) windows. The 168-hour window is our preferred specification, as it captures the full passage of the storm through the station's vicinity. Station–storm pairs are matched using a nearest-time join, and we retain only station observations recorded within 12 hours of the storm's closest approach. The resulting dataset contains approximately 14,000 station–storm observations with valid wind measurements and a comparable number with valid rainfall records, covering stations across the eastern United States.

Figure 3 plots wind speed and precipitation as functions of distance to the storm center. Panels (a) and (b) use county-level measures, while panels (c) and (d) report station-level data. The shaded region at 30–65 km marks the typical eye diameter range, where measurements are less reliable. Consistent with well-established physical patterns, wind speeds are highest in the surrounding eyewall region. As expected, wind speed declines with distance from the storm center, and we observe systematically stronger winds on the right-hand side of storms relative to the left-hand side up until a threshold of around 300km and excluding the eye of the storm. Differences between the right and left side for precipitation seem to be pronounced most in a distance band of 100-400km. In Appendix, table A.1 summarizes the descriptive statistics of weather station observations and county-level exposure measures using those distance bands. Winds are approximately 15% stronger on the right-hand side of the storm, while precipitation is about 30% heavier.

We regress wind speed and precipitation measures on a left–right indicator in Table 1. Panel (a) uses the modeled data, while panel (b) uses station data. Columns (1)–(3) report results for the full sample under alternative fixed-effect specifications, with and without county (or station) and storm fixed effects. Columns (4)–(6) replicate these regressions on a restricted sample of counties and stations with balanced exposure to left- and right-hand strikes. Results in panel (a) are statistically significant and robust across specifications. The right-hand side of storms is associated with significantly stronger winds and heavier

Figure 3: **Left–right differences in wind speed and precipitation by distance from the storm center.**

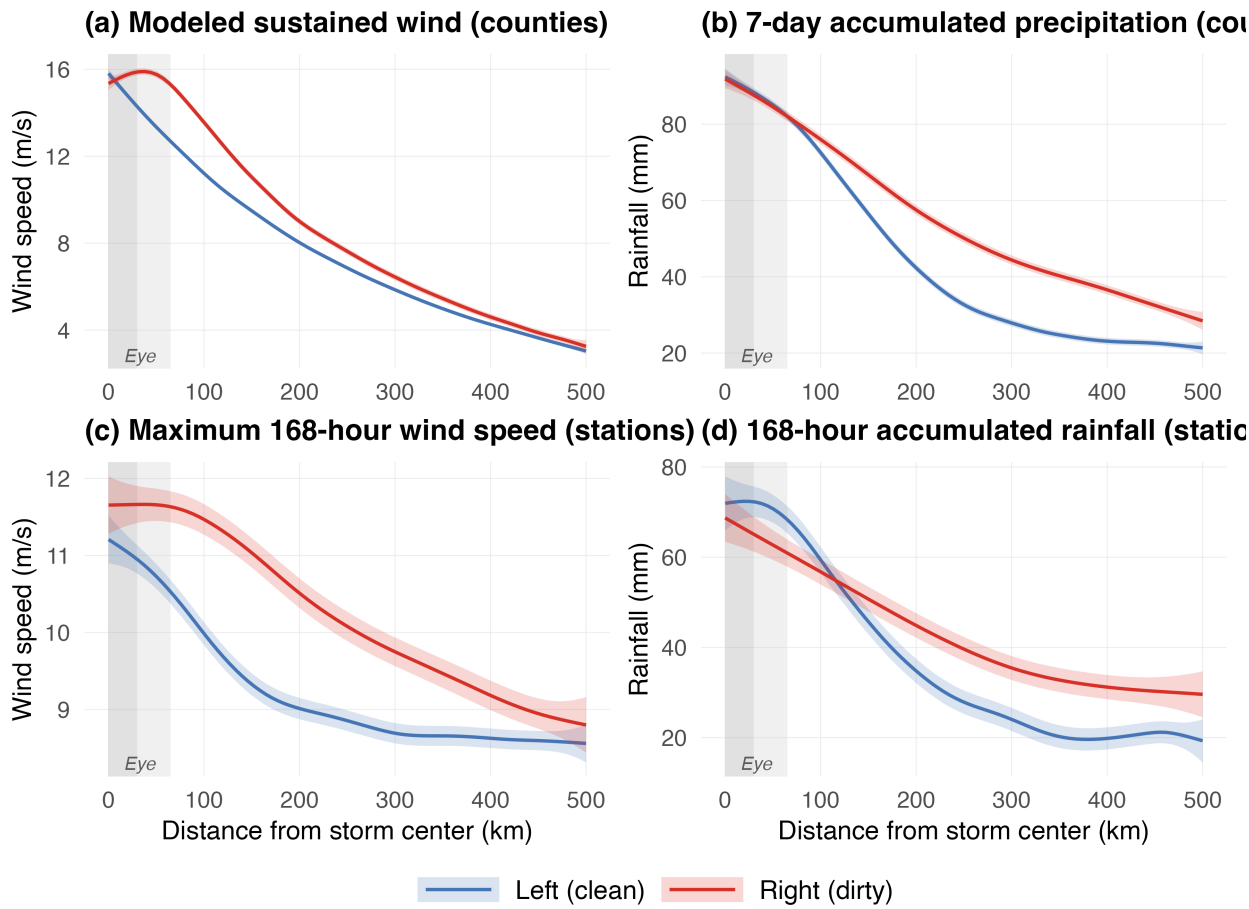

Notes: GAM smooth with 95% confidence bands for left-side (blue) and right-side (red) observations. Shaded band: typical eye diameter (30–65 km). Panels (a)–(b): county-level modeled wind and PRISM precipitation. Panels (c)–(d): station-observed wind and rainfall over 168-hour windows. *N*: (a) 92,307; (b) 90,795; (c) 14,119; (d) 14,207.

precipitation, with magnitudes consistent with the descriptive statistics. Estimates in panel (b) are very similar to those in panel (a), despite the smaller sample size.

Table 1: **OLS results for left–right differences in wind and precipitation**

	Full sample			**Balanced-exposure sample**		
	(1)	(2)	(3)	(4)	(5)	(6)
Panel A: Model data aggregated at county level						
Wind Speed (m/s) (50–300 km)						
Max 1-min sustained (continuous)	1.459***	2.592***	1.71***	2.044***	2.397***	1.862***
	(0.047)	(0.055)	(0.054)	(0.196)	(0.239)	(0.153)
Observations	42087	42087	42087	2318	2318	2318
Precipitation (mm) (100–400 km)						
PRISM 7-Day Accumulated	8.975***	19.908***	15.75***	18.668***	24.129***	22.784***
	(0.656)	(0.564)	(0.495)	(2.99)	(2.912)	(2.264)
Observations	54321	54321	54321	1470	1470	1470
Storm FE	✓	✓		✓	✓	
County FE	✓			✓		
Panel B: Weather station observations						
Wind Speed (m/s) (50–300 km)						
Maximum 168h	1.195***	1.639***	1.469***	1.23*	0.932**	1.111***
	(0.128)	(0.139)	(0.131)	(0.611)	(0.391)	(0.234)
Observations	6526	6526	6526	341	341	341
Precipitation (mm) (100–400 km)						
Accumulated 168h	6.923***	14.038***	10.384***	6.882	17.987***	14.124***
	(1.968)	(1.728)	(1.419)	(9.141)	(4.763)	(3.1)
Observations	8518	8518	8518	422	422	422
Storm FE	✓	✓		✓	✓	
Station FE	✓			✓		

Notes: Each cell reports the coefficient from a regression of the indicated outcome on the right-side indicator. Columns (1)–(3) use the full sample; columns (4)–(6) restrict to units with balanced exposure to left- and right-hand strikes. For wind speed, the distance band restriction is 50-300 km, for precipitation it is 100-400 km. Standard errors are in parentheses and clustered at the county (FIPS) level.
$^{*}p < 0.10$, $^{**}p < 0.05$, $^{***}p < 0.01$.

3.3 Impact of Bermuda High activity on wind and precipitation

As discussed in Section 3.1, left–right asymmetries are more evenly distributed across counties than overall hurricane strikes. However, they are not fully random and remain correlated with geography. We, therefore, complement this strategy by exploiting short-term fluctuations in the Bermuda High as an additional source of plausibly exogenous variation.

To track short-term movements of the Bermuda High, we use the ERA5 global atmospheric reanalysis produced by the European Center for Medium-Range Weather Forecasts (Hersbach et al., 2020), accessed through the Copernicus Climate Data Store.[7] For each storm h in our sample, we compute the average position of the BH ridge centroid during the seven days preceding landfall. This yields a storm-specific pair of coordinates for longitude and latitude $(\bar{\lambda}_h^{BH}, \bar{\varphi}_h^{BH})$.

Figure 4 plots these positions from the week-preceding landfall for all tropical cyclones in the sample. The ridge centroid longitude ranges from approximately $-71°$ to $-37°$E, with a standard deviation of 6.5°, and the latitude ranges from roughly 17° to 38°N, with a standard deviation of 4.0°. Points are colored by the cyclone's maximum wind speed, indicating that changes in BH position are not systematically correlated with storm intensity.

Relying on the variation in BH position shown in Figure 4, we construct a set of readily implementable instruments that capture shifts in the probability of tropical cyclone exposure across locations. Because winds circulate clockwise around the high, the relationship between ridge position and landfall location is nonlinear and location-specific rather than monotonic across regions.

[7] We retrieve four variables at 6-hourly temporal resolution over the period 2000–2024: mean sea level pressure (single-level), geopotential (at the 500, 700, and 850 hPa pressure levels), and the zonal and meridional components of wind (at the same three levels). From these fields, we construct a multi-dimensional set of Bermuda High indices that separately capture the strength, steering flow, and spatial position of the ridge. Strength indices consist of the area-weighted mean sea level pressure and geopotential height at each level, averaged over a core box spanning 25–35°N, 65–45°W. Steering-flow indices consist of the area-weighted zonal and meridional wind speeds at each level over the same box, along with their deep-layer mean (the simple average across the three levels). Finally, to locate the ridge, we define a broader search domain (15–45°N, 80–30°W), and at each 6-hourly time step, we identify all grid cells whose 500 hPa geopotential height exceeds the 90th percentile of the field within this domain. The area-weighted centroid of these cells yields a ridge longitude and latitude that track the position of the Bermuda High crest over time. All spatial averages use cosine-latitude weights to account for the convergence of meridians on the ERA5 latitude-longitude grid.

Figure 4: **Week-preceding Bermuda High ridge centroid position.**

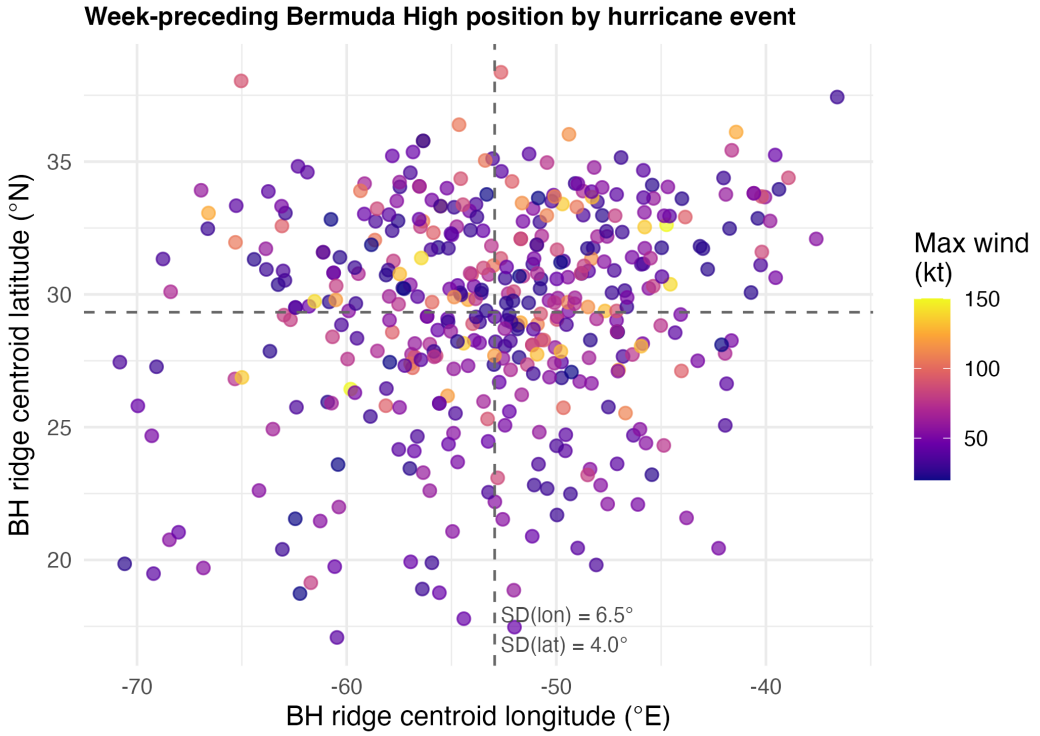

Notes: Each point is one hurricane ($N = 428$). Dashed lines: sample mean. Color: maximum sustained wind speed (knots). The spread in both dimensions confirms meaningful instrument variation across events.

To operationalize this variation, we interact state dummy variables with the average longitude and latitude of the BH ridge centroid during the seven days preceding landfall. These interactions generate plausibly exogenous cross-state differences in hurricane exposure driven by short-run steering variation.

In a 2SLS framework estimating damages as a function of sorm intensity, the exclusion restriction would require that $\bar{\lambda}_h^{BH} \times state$ and $\bar{\varphi}_h^{BH} \times state$ affect damages only through their impact on storm exposure, namely through differences in wind speed and precipitation generated by steering. Because state dummies are absorbed by finer geographic fixed effects (e.g., counties), identification arises from within-state variation in exposure induced by short-run shifts in BH position. The key assumption is that damages, such as casualties, are unrelated to last week's BH position except through its effect on realized storm intensity at a given location.

Below, we test instrument strength by predicting wind and precipitation changes as a func-

tion of the instruments. For wind speed:

$$wind_{ch} = \sum_{s=1}^{S} \delta_s^{wind} \bar{\lambda}_h^{BH} \times \mathbf{1}(c \in s) + \sum_{s=1}^{S} \pi_s^{wind} \bar{\varphi}_h^{BH} \times \mathbf{1}(c \in s) + \mu_c + \lambda_h + \nu_{ch}^{wind}, \quad (1)$$

and for precipitation:

$$precip_{ch} = \sum_{s=1}^{S} \delta_s^{precip} \bar{\lambda}_h^{BH} \times \mathbf{1}(c \in s) + \sum_{s=1}^{S} \pi_s^{precip} \bar{\varphi}_h^{BH} \times \mathbf{1}(c \in s) + \mu_c + \lambda_h + \nu_{ch}^{precip}, \quad (2)$$

where $\bar{\lambda}_h^{BH}$ and $\bar{\varphi}_h^{BH}$ are the week-preceding BH ridge longitude and latitude for hurricane h, $\mathbf{1}(c \in s)$ is a state indicator, μ_c are county fixed effects, and λ_h are hurricane fixed effects. Standard errors are clustered at the county level.[8]

We test instrument relevance with Wald F-statistics in Table 2. Each regression includes both BH longitude $\times$ state and BH latitude $\times$ state interactions (approximately 61 total regressors), with county and storm fixed effects. We report three F-statistics: the full Wald statistic testing joint significance of all 61 interactions, and partial statistics testing longitude $\times$ state and latitude $\times$ state separately, each conditional on the other set.

Both instrument dimensions are relevant. The full Wald F-statistics range from 21.0 (measured station rainfall) to 58.4 (modeled sustained wind), well above the Staiger and Stock (1997) threshold of 10. The partial F-statistics confirm that both latitude and longitude interactions contribute independently: latitude partial F-statistics range from 6.7 to 48.2, while longitude partial F-statistics range from 14.9 to 44.5. Latitude interactions are strongest for modeled wind ($F_{\text{lat}} = 48.2$ vs. $F_{\text{lon}} = 44.5$), while longitude interactions dominate for precipitation and station-level outcomes ($F_{\text{lon}} = 34.5$ vs. $F_{\text{lat}} = 26.6$ for modeled PRISM precipitation; $F_{\text{lon}} = 18.4$ vs. $F_{\text{lat}} = 10.3$ for station wind; $F_{\text{lon}} = 14.9$ vs. $F_{\text{lat}} = 6.7$ for station rainfall). The station-level F-statistics are naturally smaller due to the sparser spa-

[8]Because the instruments are BH $\times$ state interactions, one might consider clustering at the state level to account for within-state error correlation (Moulton, 1990). However, with approximately 30 states and 61 state-level parameters, the number of regressors that vary at the cluster level exceeds the number of clusters, rendering the state-clustered variance-covariance matrix singular (Cameron and Miller, 2015). County-level clustering, with over 600 clusters, avoids this problem while still accounting for serial correlation within counties across hurricanes.

tial coverage of weather stations relative to the county grid, but remain comfortably above conventional thresholds.[9]

Table 2: First-stage regressions: BH × state → physical outcomes (50–300 km band)

Outcome	N	Full F	Partial F_{lat}	Partial F_{lon}	Within-R^2
Wind speed					
Modeled max sustained (m/s)	41,783	58.4	48.2	44.5	0.043
Measured 168h max (m/s)	6,491	23.6	10.3	18.4	0.050
Precipitation					
Modeled PRISM 7-day (mm)	41,012	42.0	26.6	34.5	0.025
Measured 168h accumulated (mm)	6,528	21.0	6.7	14.9	0.018

Notes: Each row reports the first-stage regression of the indicated outcome on BH longitude × state and BH latitude × state interactions, with hurricane fixed effects throughout. Modeled rows include county fixed effects; measured (station) rows include station fixed effects. "Full F" tests joint significance of all interactions. "Partial F_{lat}" and "Partial F_{lon}" test each dimension conditional on the other. Standard errors clustered at the county level.

Figure 5 plots the state-specific latitude coefficients for wind speed (left column) and precipitation (right column), rescaled to represent the approximate percentage change in each outcome associated with a one-standard-deviation (4°, ≈444 km) northward shift in the BH ridge centroid. Panels A and B display coefficients ranked by magnitude with 95% confidence intervals; Panels C and D map the same coefficients onto the continental United States, with states whose coefficients are statistically significant at the 5% level outlined in black. For wind (Panels A, C), the pattern is uniformly positive: a northward BH shift increases modeled wind exposure in every state in the sample, with effects ranging from roughly 8% to 34%. The geographic gradient is intuitive, as states closer to the Atlantic seaboard and the Gulf coast, where hurricanes make landfall most frequently, exhibit larger responses. For precipitation (Panels B, D), the pattern is strikingly different: coefficients are mixed in sign, ranging from −14% to +69%, with roughly half individually significant, reflecting the fact that storm rainfall depends on moisture transport pathways, convergence zones, and interactions with mid-latitude frontal systems that do not simply mirror the wind field.

Figure B.1 in the Appendix maps the state-specific longitude coefficients $\hat{\delta}_s$, rescaled to approximate percentage changes per one-standard-deviation (6.5°) eastward shift in BH ridge

[9]Importantly, BH "position" should not be interpreted as inducing a simple translational shift in storm tracks. Rather, by shaping the steering flow, the ridge position affects when and where storms begin to turn around the high, implying a nonlinear mapping from BH coordinates to realized exposure.

Figure 5: **State-specific first-stage latitude coefficients.**

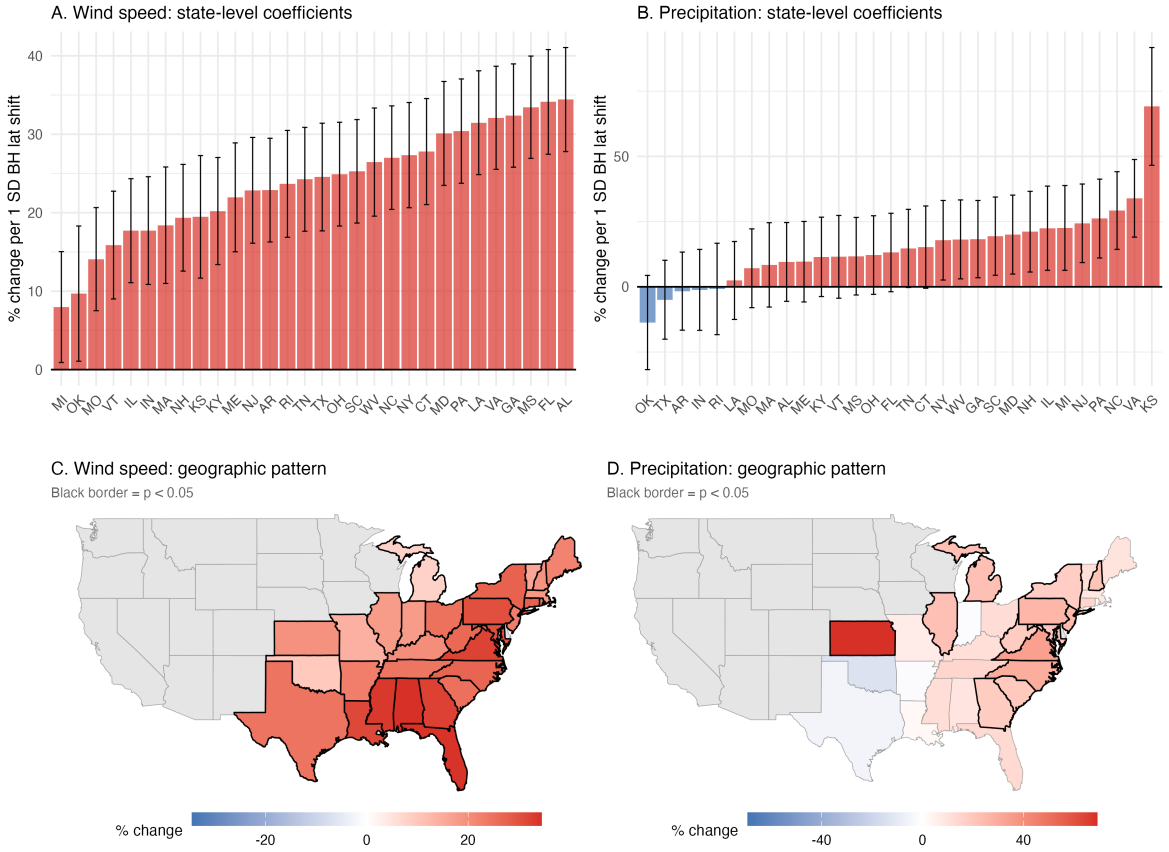

Notes: Coefficients $\hat{\pi}_s$ from equations (1)–(2), rescaled to approximate percentage change per one-standard-deviation (4°) northward shift in BH ridge latitude. Left column: modeled wind speed (log-OLS); right column: modeled precipitation (Poisson PML). Panels A–B: bar charts ranked by magnitude with 95% confidence intervals (red = positive, blue = negative). Panels C–D: geographic pattern mapped onto the continental U.S., with fill intensity proportional to coefficient magnitude; states with black borders are statistically significant at the 5% level, grey borders indicate $p \geq 0.05$. Grey-filled states have no hurricane exposure in the sample. Wind: $N = 41{,}699$, 30 states, all significant. Precipitation: $N = 41{,}012$, 30 states, 13 significant. County and storm fixed effects throughout; standard errors clustered at the county level.

longitude. Wind speed and precipitation exhibit sharply different patterns. For wind, the coefficients are uniformly negative, consistent with the physical intuition that an eastward BH shift steers storms away from the U.S. coastline, but none of the 31 state-level estimates is individually significant at the 5% level. This near-uniform response explains why the joint Wald test rejects the null while individual coefficients are imprecise: east-west shifts move all storm tracks in the same direction, producing a near-uniform effect that is largely absorbed by the hurricane fixed effect. For precipitation, by contrast, 22 of 30 state-level longitude coefficients are individually significant, with substantial heterogeneity in both sign and magnitude. This reflects the fact that east-west BH shifts alter moisture transport pathways and convergence zones in state-specific ways that survive the storm fixed effect. The contrast with the latitude coefficients (Figure 5), where all 30 wind coefficients but only 13 of 30 precipitation coefficients are individually significant, underscores a complementarity between the two instrument dimensions: latitude interactions primarily identify wind variation, while longitude interactions are more informative for precipitation.

3.4 Calibration of Bermuda High instruments

With 31 states and two ridge-centroid coordinates, many-instruments bias is a concern (Bound et al., 1995). Below, we present strategies to reduce the number of instruments, which we will implement in robustness checks when estimating damage responses in future versions of the paper.

To halve the number of instruments, we can treat longitude $\times$ state interactions as controls rather than instruments, reducing the identifying set to the 30 BH latitude $\times$ state interactions. We can also implement two complementary reductions. First, we can restrict the sample to the 10 states with the largest $|t|$-statistics in the wind first stage. Alternatively, we can aggregate instruments into four broader regions: Gulf, South Atlantic, North Atlantic, and Inland states.

Table 3 reports the partial Wald F-statistics for the latitude instruments and the within-R^2 for each instrument set and outcome. The trade-off is between first-stage strength and exposure to many-instruments bias. For the modeled outcomes, partial F-statistics exceed 10

across all specifications. The station-level outcomes show weaker first stages under reduction, particularly the top-10 subset ($F < 10$), reflecting the sparser spatial coverage of weather stations. The regional grouping performs better for station wind ($F = 19.9$) but is weak for station rainfall ($F = 1.8$), suggesting that the BH–precipitation relationship is more heterogeneous and harder to capture with coarse geographic aggregation.

Table 3: Instrument reduction: partial first-stage F-statistics by instrument set

Outcome	Instrument set	N	K_{lat}	Partial F	Within-R^2
Modeled max sustained wind	Full (all states)	41,783	30	48.2	0.043
	Top-10 states	25,007	10	11.6	0.011
	Regional (4 groups)	41,783	3	217.8	0.024
Measured 168h max wind	Full (all states)	6,491	34	10.3	0.050
	Top-10 states	3,533	9	0.9	0.011
	Regional (4 groups)	6,425	3	19.9	0.017
Modeled PRISM precipitation	Full (all states)	41,012	30	26.6	0.025
	Top-10 states	18,305	10	17.5	0.022
	Regional (4 groups)	41,012	3	64.2	0.008
Measured 168h rain	Full (all states)	6,528	34	6.7	0.018
	Top-10 states	3,556	9	3.0	0.012
	Regional (4 groups)	6,462	3	1.8	0.003

Notes: Partial Wald F-statistic for joint significance of BH latitude interactions, conditional on BH longitude interactions as controls. Modeled rows include county and hurricane FE; measured (station) rows include station and storm FE. Standard errors clustered at the county level. "Top-10 states" are ranked by $|t|$ from the wind first stage of the respective data source. "Regional" groups states into Gulf, South Atlantic, North Atlantic, and Inland.

Overall, the F-statistics reported in Table 2 are large. In Table 3, they exceed the conventional threshold of 10 for all modeled variables. Together, these results indicate that the instruments are sufficiently strong to explain variation in storm intensity.

4 Conclusion

We aim to exploit spatial asymmetries in storm dynamics to causally identify how damages vary with intensity. In this preliminary draft, we establish two complementary sources of plausibly exogenous variation in hurricane exposure: within-storm left–right wind asymmetries and short-run steering shifts in the Bermuda High. We document that these physical mechanisms generate strong and economically meaningful differences in local wind and pre-

cipitation intensity. In future iterations, we will use these mechanisms for a causal estimation of how damages scale with tropical cyclone intensity and for assessing the curvature of the storm damage function.

References

Anderson B., Schumacher A., Guikema S., Quiring S., Ferreri J., Tennant E., and Robinson J. (2021) *stormwindmodel: Model Tropical Cyclone Wind Speeds*, R package version 0.1.5.9 (2021-05-17), commit 03e80bebdb96e9f24978e1174218c7b2688f8516.

Barone G. and Mocetti S. (2014) Natural Disasters, Growth and Institutions: A Tale of Two Earthquakes. *Journal of Urban Economics*, 84: 52–66.

Barrage L. and Nordhaus W. (2024) Policies, Projections, and the Social Cost of Carbon: Results from the DICE-2023 Model. *Proceedings of the National Academy of Sciences*, 121(13): e2312030121.

Bound J., Jaeger D. A., and Baker R. M. (1995) Problems with Instrumental Variables Estimation When the Correlation Between the Instruments and the Endogenous Explanatory Variable is Weak. *Journal of the American Statistical Association*, 90(430): 443–450.

Cameron A. C. and Miller D. L. (2015) A Practitioner's Guide to Cluster-Robust Inference. *Journal of Human Resources*, 50(2): 317–372.

Cappucci M. and Noll B. (2025) Why This Weather Feature Has so Much Influence on a Hurricane's Path. *The Washington Post*.

Cashin P., Mohaddes K., and Raissi M. (2017) Fair Weather or Foul? The Macroeconomic Effects of El Niño. *Journal of International Economics*, 106: 37–54.

Cavallo E. A. and Noy I. (2010) The Economics of Natural Disasters: A Survey. https://publications.iadb.org/en/publications/english/viewer/The-Economics-of-Natural-Disasters-A-Survey.pdf.

Center for Climate and Energy Solutions (2026) Hurricanes and Climate Change.

Chan J. C. (2005) The Physics of Tropical Cyclone Motion. *Annual Review of Fluid Mechanics*, 37(1): 99–128.

Deryugina T. (2017) The Fiscal Cost of Hurricanes: Disaster Aid versus Social Insurance. *American Economic Journal: Economic Policy*, 9(3): 168–198.

Diem J. E. (2013) Influences of the Bermuda High and Atmospheric Moistening on Changes in Summer Rainfall in the Atlanta, Georgia Region, USA. *International Journal of Climatology*, 33(1): 160–172.

Dietz S. and Stern N. (2015) Endogenous Growth, Convexity of Damage and Climate Risk: How Nordhaus' Framework Supports Deep Cuts in Carbon Emissions. *The Economic Journal*, 125(583): 574–620.

Hart E. M. and Bell K. (2015) *prism: Download Data from the Oregon PRISM Project*, R package version 0.3.0.

Hersbach H., Bell B., Berrisford P., Hirahara S., Horányi A., Muñoz-Sabater J., Nicolas J., Peubey C., Radu R., Schepers D., Simmons A., Soci C., Abdalla S., Abellan X., Balsamo G., Bechtold P., Biavati G., Bidlot J., Bonavita M., De Chiara G., Dahlgren P., Dee D., Diamantakis M., Dragani R., Flemming J., Forbes R., Fuentes M., Geer A., Haimberger L., Healy S., Hogan R. J., Hólm E., Janisková M., Keeley S., Laloyaux P., Lopez P., Lupu C., Radnoti G., de Rosnay P., Rozum I., Vamborg F., Villaume S., and Thépaut J.-N. (2020) The ERA5 Global Reanalysis. *Quarterly Journal of the Royal Meteorological Society*, 146(730): 1999–2049.

Holland G. and Bruyère C. L. (2014) Recent Intense Hurricane Response to Global Climate Change. *Climate Dynamics*, 42(3): 617–627.

Holland G. J. (1980) An Analytic Model of the Wind and Pressure Profiles in Hurricanes. *Monthly Weather Review*, 108(8): 1212–1218.

Karbownik K. and Wray A. (2019) Long-Run Consequences of Exposure to Natural Disasters. *Journal of Labor Economics*, 37(3): 949–1007.

Kellenberg D. and Mobarak A. M. (2011) The Economics of Natural Disasters. *Annual Review of Resource Economics*, 3(1): 297–312.

Knowles J. T. and Leitner M. (2007) Visual Representations of the Spatial Relationship Between Bermuda High Strengths and Hurricane Tracks. *Cartographic Perspectives*(56): 37–51.

Krieger N. (2023) *USpopcenters: United States Centers of Population (Centroids)*, R package version 0.2.0.

Landsea C. W. and Franklin J. L. (2013) Atlantic Hurricane Database Uncertainty and Presentation of a New Database Format. *Monthly Weather Review*, 141(10): 3576–3592.

Lugo A. E. (2000) Effects and Outcomes of Caribbean Hurricanes in a Climate Change Scenario. *Science of The Total Environment*, 262(3): 243–251.

Masiero G. and Santarossa M. (2021) Natural Disasters and Electoral Outcomes. *European Journal of Political Economy*, 67: 101983.

Moulton B. R. (1990) An Illustration of a Pitfall in Estimating the Effects of Aggregate Variables on Micro Units. *The Review of Economics and Statistics*, 72(2): 334–338.

Mudd L., Wang Y., Letchford C., and Rosowsky D. (2014) Assessing Climate Change Impact on the U.S. East Coast Hurricane Hazard: Temperature, Frequency, and Track. *Natural Hazards Review*, 15(3): 04014001.

NASA (2022) A Force of Nature: Hurricanes in a Changing Climate.

National Hurricane Center (2026) Saffir-Simpson Hurricane Wind Scale. https://www.nhc.noaa.gov/aboutsshws.php.

NOAA National Centers for Environmental Information (2025) U.S. Billion-dollar Weather and Climate Disasters.

NOAA National Hurricane Center (2024) North Atlantic Hurricane Database (HURDAT2). Best-track data for the North Atlantic basin, accessed 2025-03-06.

Nordhaus W. (2018) Projections and Uncertainties about Climate Change in an Era of Minimal Climate Policies. *American economic journal: economic policy*, 10(3): 333–360.

Paudel J. and Ryu H. (2018) Natural Disasters and Human Capital: The Case of Nepal's Earthquake. *World Development*, 111: 1–12.

Powell M. D., Vickery P. J., and Reinhold T. A. (2003) Reduced Drag Coefficient for High Wind Speeds in Tropical Cyclones. *Nature*, 422(6929): 279–283.

PRISM Climate Group (2024) PRISM Gridded Climate Data: Daily Precipitation (4 km Resolution).

Roth Tran B. and Wilson D. J. (2025) The Local Economic Impact of Natural Disasters. *Journal of the Association of Environmental and Resource Economists*, 12(6): 1667–1704.

Sheldon T. L. and Zhan C. (2019) The Impact of Natural Disasters on US Home Ownership. *Journal of the Association of Environmental and Resource Economists*, 6(6): 1169–1203.

Smith A., Lott N., and Vose R. (2011) The Integrated Surface Database: Recent Developments and Partnerships. *Bulletin of the American Meteorological Society*, 92(6): 704–708.

Staiger D. and Stock J. H. (1997) Instrumental Variables Regression with Weak Instruments. *Econometrica*, 65(3): 557–586.

Uhlhorn E. W., Klotz B. W., Vukicevic T., Reasor P. D., and Rogers R. F. (2014) Observed Hurricane Wind Speed Asymmetries and Relationships to Motion and Environmental Shear. *Monthly Weather Review*, 142(3): 1290–1311.

U.S. Census Bureau (2011) Centers of Population Computation for the United States, 1950–2010. Technical Report COP2010 Documentation, U.S. Department of Commerce, Geography Division, Washington, DC.

——— (2018) 2018 Cartographic Boundary File: United States Counties (1:500,000). cb_2018_us_county_500k.zip.

Wang Bin R. L., Yuqing W., and Liguang W. (1999) Dynamics in Tropical Cyclone Motion: A Review. *Chinese Journal of Atmospheric Sciences*, 22(4): 416–434.

Weitzman M. L. (2012) GHG Targets as Insurance Against Catastrophic Climate Damages. *Journal of Public Economic Theory*, 14(2): 221–244.

Willoughby H. E., Darling R. W. R., and Rahn M. E. (2006) Parametric Representation of the Primary Hurricane Vortex. Part II: A New Family of Sectionally Continuous Profiles. *Monthly weather review*, 134(4): 1102–1120.

Xiao Y. (2011) Local Economic Impacts of Natural Disasters*. *Journal of Regional Science*, 51(4): 804–820.

Zhu J. and Liang X.-Z. (2013) Impacts of the Bermuda High on Regional Climate and Ozone over the United States. *Journal of Climate*, 26(3): 1018–1032.

Online Appendix

A Summary statistics

Table A.1: Summary statistics of storm-related weather exposure.

	Full sample				Balanced-exposure sample			
	Left	Right	Diff	p	Left	Right	Diff	p
Panel A: Model data aggregated at county level								
Wind Speed (m/s) (50-300km)								
Max 1-min sustained (continuous)	8.71	10.42	-1.71	$< 1\%$	8.21	10.07	-1.86	$< 1\%$
Observations	26,130	15,957			1,159	1,159		
Precipitation (mm) (100-400km)								
PRISM 7-Day Accumulated	36.31	52.06	-15.75	$< 1\%$	32.86	55.65	-22.78	$< 1\%$
Observations	35,057	19,264			733	737		
Panel B: Weather station observations								
Wind Speed (m/s) (50-300km)								
Maximum 168h	9.32	10.79	-1.47	$< 1\%$	9.62	10.73	-1.11	$< 1\%$
Observations	3,977	2,549			173	168		
Precipitation (mm) (100-400km)								
Accumulated 168h	30.39	40.77	-10.38	$< 1\%$	30.49	44.62	-14.12	$< 1\%$
Observations	5,324	3,194			212	210		

B Longitude by state instruments

Figure B.1 maps the state-specific longitude coefficients $\hat{\delta}_s$ from equations (1)–(2), rescaled to approximate percentage changes per one-standard-deviation (6.5°) eastward shift in BH ridge longitude. The two outcomes exhibit sharply different patterns. For wind speed, all 31 coefficients are negative, consistent with an eastward BH shift steering storms away from the U.S. coastline, but none reaches individual significance at the 5% level. This near-uniform response explains why longitude interactions are collectively predictive (the joint Wald test rejects the null) but individually imprecise: the hurricane fixed effect absorbs most of the common eastward-shift signal. For precipitation, by contrast, 22 of 30 state-level longitude coefficients are individually significant, with heterogeneous signs and magnitudes reflecting the state-specific effects of east-west BH shifts on moisture transport pathways and convergence zones.

Figure B.1: **State-specific first-stage longitude coefficients.**

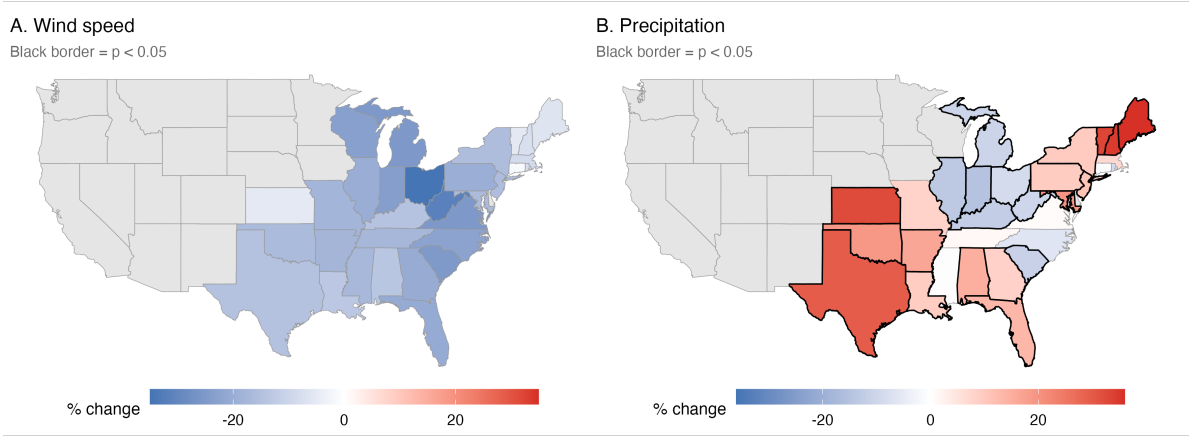

Notes: Coefficients $\hat{\delta}_s$ from equations (1)–(2), rescaled to approximate percentage change per one-standard-deviation (6.5°) eastward shift in BH ridge longitude. Panel A: modeled wind speed (log-OLS); Panel B: modeled precipitation (Poisson PML). Fill intensity is proportional to coefficient magnitude; states with black borders are statistically significant at the 5% level. Grey-filled states have no storm exposure in the sample. Wind: 31 states, 0 individually significant. Precipitation: 30 states, 22 individually significant. County and storm fixed effects throughout; standard errors clustered at the county level.